



Interfacial charge transfer in 0D/2D defect-rich heterostructures for efficient solar-driven CO₂ reduction

Hainan Shi^a, Saran Long^a, Shen Hu^a, Jungang Hou^{a,*}, Wenjun Ni^a, Chunshan Song^{a,b}, Keyan Li^{a,*}, Gagik G. Gurzadyan^a, Xinwen Guo^{a,*}

^a State Key Laboratory of Fine Chemicals, PSU-DUT Joint Center for Energy Research, School of Chemical Engineering, Dalian University of Technology, Dalian, 116024, PR China

^b EMS Energy Institute, PSU-DUT Joint Center for Energy Research and Department of Energy & Mineral Engineering, Pennsylvania State University, University Park, Pennsylvania 16802, United States



ARTICLE INFO

Keywords:
0D/2D heterostructures
Oxygen vacancy
TiO₂ quantum dots
Charge transfer
Solar CO₂ reduction

ABSTRACT

Two-dimensional graphitic carbon nitride ($\text{g-C}_3\text{N}_4$) has been widely explored as a promising photocatalyst for solar CO₂ conversion. However, rapid charge recombination and low visible-light utilization are severely detrimental to photocatalytic CO₂ conversion. Zero-dimensional/two-dimensional (0D/2D) heterostructures are considered the promising materials with size tunability and enhanced charge separation efficiency for photocatalysis. Herein, a 0D/2D heterostructure of oxygen vacancy-rich TiO₂ quantum dots confined in $\text{g-C}_3\text{N}_4$ nanosheets ($\text{TiO}_{2-x}/\text{g-C}_3\text{N}_4$) was prepared by in-situ pyrolysis of NH₂-MIL-125 (Ti) and melamine. Charge dynamics analysis by time-resolved photoluminescence (tr-PL) and femtosecond and nanosecond pump-probed transient absorption (TA) spectra revealed that charges transfer occurred from 2D- $\text{g-C}_3\text{N}_4$ to 0D-TiO₂ at an ultrafast sub-picosecond time scale (< 1 ps) through the intimate interface. The overall fast decay of the charge carriers was attributed to interfacial charge transfer, which was accompanied by recombination relaxation mediated by shallow trapped sites. Ultrafast interfacial charge transfer greatly promoted charge separation and electrons in shallow trapped sites were easily trapped by CO₂. In addition, combining with the synergistic advantage of strong visible light absorption, high CO₂ adsorption and large surface area, $\text{TiO}_{2-x}/\text{g-C}_3\text{N}_4$ exhibited a superior CO evolution rate of 77.8 $\mu\text{mol g}^{-1} \text{h}^{-1}$, roughly 5 times that of pristine $\text{g-C}_3\text{N}_4$ (15.1 $\mu\text{mol g}^{-1} \text{h}^{-1}$). This work provides in-depth insights into optimizing the heterojunction for robust solar CO₂ conversion.

1. Introduction

Increasing concerns about global energy and CO₂ emission issues call for the development of new clean sustainable technologies. Solar-driven CO₂ conversion to chemical fuels is a promising approach to address energy and environmental demands because of without requirement for high pressures and/or temperatures [1–5]. The design and synthesis of suitable photocatalysts is of great importance for accomplishing CO₂ reduction under visible light irradiation. Favorable alternative photocatalysts for CO₂ conversion need to meet the following requirements: (i) absorption and utilization of broad visible light; (ii) sufficient negative potential for CO₂ reduction; (iii) efficient separation and transfer of photoinduced electrons and holes; (iv) excellent CO₂ adsorption ability [6,7]. Two-dimensional (2D) metal-free semiconductor graphitic carbon nitride ($\text{g-C}_3\text{N}_4$) has been extensively investigated and applied in photocatalytic water splitting and CO₂

reduction as a heterogeneous photocatalyst since the first report of photocatalytic in 2009 due to its earth-abundance, low-toxicity, facile synthesis, good stability, and appropriate band gap to various reduction/oxidation reactions under visible light [8–14]. However, pristine $\text{g-C}_3\text{N}_4$ still has the drawbacks of low surface area, insufficient visible-light absorption, low CO₂ adsorption volume, and most importantly, rapid recombination of photoexcited charge carriers, which leads to unsatisfactory photocatalytic activity. Many strategies on modification of $\text{g-C}_3\text{N}_4$ are proposed aiming to improving its properties such as morphology control [15–17], doping [18], crystallinity [12,19] and pore structure improvement [20,21], optical quality change [22] and so on. As an alternative strategy for promoting charge separation to enhance photocatalytic performance, it is promising for combining solid-state semiconductors with diverse band gaps, especially constructing heterostructures in the interface [7,23,24].

Among various heterostructures, conventional composites of TiO₂/

* Corresponding authors.

E-mail addresses: jhou@dlut.edu.cn (J. Hou), keyanli@dlut.edu.cn (K. Li), guoxw@dlut.edu.cn (X. Guo).

$\text{g-C}_3\text{N}_4$ have been extensively applied in the photocatalysis field due to their outstanding photocatalytic performance [25]. A variety of strategies for constructing $\text{TiO}_2/\text{g-C}_3\text{N}_4$ heterostructures have been investigated, including core-shell structure [26–28], ordered nanotube arrays [29], porous/hollow microspheres heterojunctions [24,30,31] and so on. However, few reports on $\text{TiO}_2/\text{g-C}_3\text{N}_4$ heterostructures have aimed to integrate zero-dimensional (0D) quantum dots (QDs) and two-dimensional (2D) nanosheets. 0D QDs have received extensive attention due to their unique virtues of small size ($< 10 \text{ nm}$), short charge transfer path and strongly size-dependent optical and electrical properties [32,33]. Given these advantages, loading 0D QDs on the 2D nanosheets to construct 0D/2D heterostructures could be an efficient way to promote charge separation. Previous reports mentioned that 0D QDs can act as the channel for acceptance of charge carriers from 2D materials to facilitate charge transfer and then suppress the recombination of photoinduced charges [34]. Recently, 0D/2D heterostructures have become attractive materials due to their outstanding optical properties and advantages of easy preparation, strong visible light-responsive range, less-constrained interfacial states and superior interfacial charge transfer capacity for photocatalytic/photoelectronic applications [35–38]. For example, Ma and co-workers [35] loaded vanadate QDs on $\text{g-C}_3\text{N}_4$ nanosheets, which exhibited superior photocatalytic performance. Wang et al. [36] constructed 0D/2D heterostructures of Co_3O_4 QDs/ TiO_2 nanobelt, which exhibited excellent photocatalytic overall water splitting without noble metals. However, an in-depth understanding of the interfacial charge behavior in 0D/2D heterostructures is still lacking. Moreover, a diversity of strategies for preparing heterostructures of 0D QDs loaded on 2D nanosheets have been reported, such as the chemical reaction route [35,39], hydrothermal method [36] and sonication approach [40]. However, insights on QDs/nanosheets heterostructures based on an in-situ pyrolysis approach by means of metal organic frameworks (MOFs) have rarely been reported. It is well known that most of MOFs materials themselves are promising semiconductors applied in photoredox catalysis [41]. Importantly, MOFs have been intensely explored as an ideal precursor or template for preparing metal oxide nanoparticles with highly porous structure and large surface areas by a facile pyrolysis process [42–46]. Based on the analysis above, it is desirable to construct 0D/2D $\text{TiO}_2/\text{g-C}_3\text{N}_4$ heterostructure by a facile in-situ MOF pyrolysis approach. In addition, it is essential to explore the interfacial charge behavior of the 0D/2D heterostructures to obtain a further in-depth understanding of the mechanism of photocatalytic CO_2 reduction performance.

Herein, 0D/2D heterojunctions of oxygen vacancy-rich TiO_2 QDs confined in $\text{g-C}_3\text{N}_4$ nanosheets were prepared by in situ pyrolysis of MIL-125-NH₂ (Ti) and melamine. The core idea of this work is to efficiently separate photogenerated charge carriers by building the heterostructure interface. Charge dynamics analysis by time-resolved photoluminescence (tr-PL) and transient absorption (TA) spectra revealed that charge transfer takes place from 2D- $\text{g-C}_3\text{N}_4$ to 0D- TiO_2 within $< 1 \text{ ps}$ through the intimate interface. The overall fast decay of charge carriers was attributed to charge transfer accompanied by the recombination relaxation mediated by shallow trapped sites, which greatly promoted charge separation and thus enhanced photocatalytic activity. Based on these features of enhanced visible light absorption, large surface area, increased CO_2 adsorption and efficient charge separation, the as-synthesized $\text{TiO}_{2-x}/\text{g-C}_3\text{N}_4$ exhibited superior photocatalytic CO_2 reduction activity compared with pristine $\text{g-C}_3\text{N}_4$. Thus, this work provides a platform for the design of 0D/2D heterostructures and a deep understanding of the mechanism of charge dynamics for energy conversion.

2. Experimental

2.1. Preparation of 0D/2D heterostructure of QDs TiO_2 confined in $\text{g-C}_3\text{N}_4$ nanosheets

Melamine was purchased from Beijing Chemical Reagent Corp., PR China. Nitric acid was obtained from Aladdin Reagent Corp. 2-Amino-1,4-benzenedicarboxylic acid (NH₂-BDC), titanium(IV) isopropoxide ($\text{C}_{12}\text{H}_{28}\text{O}_4\text{Ti}$, TOPT) were purchased from Aldrich. N, N-Dimethylformamide (DMF) and methanol (CH₃OH) were obtained from Shanghai Chemical Reagent Inc. All chemicals were used as received without further purification.

$\text{g-C}_3\text{N}_4$ was synthesized by a one-step thermal-polymerization of melamine. In detail, 5 g of melamine was placed in a crucible with a cover and then heated to 550 °C for 3 h at a heating rate 5 °C /min in a muffle furnace under the air atmosphere. After calcination, the as-prepared power was milled and collected, which was denoted as MCN.

Preparation of synthesis of NH₂-MIL-125(Ti) and M-TiO₂: 0.56 g NH₂-BDC was dissolved in a 40 mL mixture of DMF and CH₃OH (4:1, v/v) with the aid of ultrasonication. Afterward, 600 uL of titanium (IV) isopropoxide (TPOT) was added dropwise into the above mixture. Then, the mixture was put into a 100 mL Teflon lined stainless steel autoclave and heated at 423 K for 24 h in an oven. After reaction, the yellow-green precipitates were collected by centrifugation, washed with DMF and methanol three times, and dried at 60 °C under vacuum. TiO₂ derived from NH₂-MIL-125(Ti) was prepared by directly calcinating NH₂-MIL-125(Ti) in the air. In detail, 1 g NH₂-MIL-125(Ti) was put into a crucible and then heated to 500 °C for 2 h with a heating rate 5 °C /min in a muffle furnace. The obtained white power was collected, which was denoted as M-TiO₂.

0D/2D heterostructures of QDs TiO_2 confined in $\text{g-C}_3\text{N}_4$ nanosheets were prepared by in-situ pyrolysis of the mixture of melamine and NH₂-MIL-125(Ti) with different mass ratio. The mixture in an alumina crucible with a cover was heated to 550 °C for 3 h at a heating rate of 5 °C /min in a muffle furnace under the air atmosphere. The obtained products were milled and collected and then put in a crucible without any cover and heated at 450 °C for another 2 h at a heating rate of 5 °C /min in a muffle furnace under the air atmosphere. The precursor ratio of the melamine and NH₂-MIL-125(Ti) with mass ratio (g/g) of 5:0.05, 5:0.1, 5:0.15 and 5:0.4 were used to synthesize the $\text{TiO}_{2-x}/\text{MCN}$ heterostructures, and the relevant products were denoted as $y\text{TiO}_{2-x}/\text{MCN}$ ($y = 1, 2, 3$ and 8, which is equal to the percentage of Ti-MOF out of melamine). The mixture of precursors was just heated at 550 °C for 3 h or 5 h without 450 °C heat treatment under other conditions unchanged, the products denoted as $\text{TiO}_2/\text{MCN}-x$ ($x = 3$ and 5).

In contrast, similar synthesis method of $\text{TiO}_2/\text{g-C}_3\text{N}_4$ was carried out. Briefly, the mixture of a certain amount of the M-TiO₂ and melamine was put into a crucible with a cover and then heated at 550 °C for 3 h at a heating rate 5 °C /min in a muffle furnace under the air atmosphere. The M-TiO₂ dosage was equal to the amount of 2% MOF out of melamine in the air, which was denoted as 2TiO₂-MCN. The M-TiO₂ amount was estimated according to the TGA result of NH₂-MIL-125 (Ti) (Fig. S1).

2.2. Characterization

Scanning electron microscopy (SEM) images were obtained on a Hitachi SU8220 instrument with an acceleration voltage of 5 kV. Transmission electron microscope (TEM) images were taken on a Tecnai G220 S-twin instrument (FEI Company). X-ray diffraction (XRD) patterns were recorded on a Smart Lab 9 X-ray diffractometer (Rigaku Corporation). Fourier transform infrared (FT-IR) spectra were measured using an EQUINOX55 FT-IR spectrometer. X-ray photoelectron spectroscopy (XPS) spectra were recorded on a Thermo VG ESCALAB250 instrument. The nitrogen sorption isotherms were measured with a Quantachrome autosorb-iQ2 gas adsorption analyzer at 77 K. UV-vis

spectra were taken on a JASCO V-550 spectrometer. Gas Chromatography/Mass Spectrometer was carried out on a Agilent 5975C instrument. Photoluminescence (PL) spectra were acquired on a JASCO FP-6200 spectrofluorometer with the excitation wavelength at 310 nm. The electron paramagnetic resonance (EPR) was carried out at room temperature on an A220-9.5/12 (Bruker). UV Raman spectra were recorded using a home-made triple stage UV Raman spectrograph with a spectral resolution of 2 cm^{-1} . The laser line at 325 nm of an He:Cd laser was used as the exciting source with an output of 30 mW. The power of the laser at samples was about 3 mW. Time-resolved photoluminescence (tr-PL) measurements were carried out at room temperature by the time-correlated single photon counting (TCSPC) technique (PicoQuant PicoHarp 300). By use of deconvolution/fit program (PicoQuant FluFit) the time resolution was reached down to 10 ps. The second harmonic of a titanium – sapphire laser (Mai Thai DeepSee) at 350 nm (150 fs, 80 MHz) was used as the excitation source.

2.3. Photocatalytic test

Photocatalytic CO₂ reduction experiment was conducted in a 43 mL quartz vessel with a rubber septum at the temperature of 25 °C carried out by circulation cooling system. The visible light was provided by using a 300 W Xenon lamp (PLS-SXE300C, Beijing Perfectlight Co. Ltd., China) coupled to a UV cut-off filter ($\lambda > 400 \text{ nm}$). In a typical experiment, 5 mg photocatalyst was dispersed in 5 mL of solution containing 4 mL of methyl cyanide (MeCN) solvent, 1 mL of triethanolamine (TEOA), bipyridine (bpy) (10 mmol/L) and 25 μL of 20 mmol/L CoCl₂ aq. The mixture system was subjected to ultrasound treatment for 30 min, purged by CO₂ (99.999%) for 30 min to remove air and then was sealed. The produced gases (H₂ and CO) were detected with a syringe every 1 h by the gas Chromatograph equipped with TCD detector and FID detector connection in series (C molecular sieve column) methane reforming furnace. Argon was used as the carrier gas.

3. Results and discussion

3.1. Catalyst synthesis and characterization

0D/2D heterostructures of oxygen-deficient TiO₂ quantum dots confined in g-C₃N₄ nanosheets (TiO_{2-x}/MCN) were prepared through in-situ two-step pyrolysis of Ti-MOF and melamine as illustrated in Fig. 1a. For comparison, another composite of TiO₂/g-C₃N₄ (TiO₂-MCN) was also prepared by thermal treatment of the mixture of melamine and TiO₂ from Ti-MOF, as shown in Scheme S1 (Supporting Information). Scanning electron microscope (SEM) images demonstrate that the TiO₂ derived from MOF (M-TiO₂) retains the well-defined disk-shape morphology of Ti-MOF (Fig. 1b and Fig. S2). The disk-shape of TiO₂ is also observed in the 2TiO₂-MCN (Fig. S3b and S4e, f). However, the disk-shape of TiO₂ disappears in the TiO_{2-x}/g-C₃N₄. Instead, TiO_{2-x}/MCN displays a curly sheet-like morphology and appears more loosely connected (Fig. 1c) than the pristine g-C₃N₄ (MCN) (Fig. S3a). Transmission electron microscopy (TEM) images further confirm the sheet-like shape in TiO_{2-x}/MCN (Fig. 1d). High-resolution TEM (HRTEM) images (Fig. 1e, f) show that a large number of quantum dots with a uniform size of $\approx 5 \text{ nm}$ are homogeneously anchored on the surface of the nanosheets. The clear lattice fringes 0.35 nm from the quantum dots are indexed to the (101) plane of anatase TiO₂ (Fig. 1g). In addition, energy dispersive X-ray (EDX) elemental mapping images disclose that the Ti and O elements are homogeneously supported on the surface of the g-C₃N₄ (Fig. 1h–l). By contrast, the TiO₂/g-C₃N₄ prepared by one-step calcination for different time also display the bulk shape morphology similar to that of pristine g-C₃N₄ (Fig. S3c, d). No obvious TiO₂ particles (Fig. S4a, b) or aggregated large TiO₂ particles with low crystallinity (Fig. S4c, d) are observed on the surface of the g-C₃N₄, thus demonstrating that prolonged calcination time and sufficient oxygen are necessary for crystal phase formation and uniform dispersion of TiO₂.

nano-particles.

X-ray diffraction (XRD) patterns of pristine g-C₃N₄ and TiO₂/g-C₃N₄ composites are shown in Fig. 2a. Two typical diffraction peaks at 13.1° and 27.4° in the pristine g-C₃N₄ are ascribed to in-plane packing of tri-s-triazine motifs ((001) plane) and layered interfacial stacking of the conjugated tri-s-triazine structure ((002) plane), respectively [47]. M-TiO₂ exhibits well-defined peaks at 25.3°, 37.8°, and 47.9, indexed to the (101), (004), (200) crystal planes of anatase TiO₂ (JCPDS card no. 21-1272). Similar diffraction peaks of MCN and M-TiO₂ with lower intensity are also observed in yTiO_{2-x}/MCN ($y = 1, 2, 3$ and 8, mass percentage of Ti-MOF out of melamine) and 2TiO₂-MCN, indicating successful synthesis of the composites of g-C₃N₄ and TiO₂ via co-pyrolysis of melamine and Ti-MOF. Obviously, the intensities of peaks located at 27.2° for yTiO_{2-x}/MCN and 2TiO₂-MCN are much lower than that of the pristine g-C₃N₄, indicating that the introduction of Ti-MOF influences the condensation of melamine leading to the loss of ordered structure within the framework. Compared with 2TiO_{2-x}/MCN, no obvious diffraction peaks belonging to TiO₂ are observed for TiO₂/MCN for one-step pyrolysis (Fig. S5), indicating that TiO₂ particles remain in the amorphous phase even when the calcination time was prolonged to 5 h, in consistent with the TEM results. The structures of the composites were further confirmed by Raman spectroscopy (Fig. S6). The typical Raman shift at 143 cm^{-1} is ascribed to the lattice vibration of M-TiO₂ crystal. The Raman shifts located at 708 and 765 cm^{-1} are assigned to the in-plane bending vibrations of C=N=C linked heptazine rings; the peak at 975 cm^{-1} is due to the symmetric N–breathing mode of tri-s-triazine units of g-C₃N₄ [48]. The yTiO_{2-x}/MCN showed the characteristic peaks of TiO₂ and g-C₃N₄, indicating the successful formation of TiO₂/g-C₃N₄ composites.

Fourier transform infrared (FT-IR) spectroscopy was performed to further confirm the bonding structure of yTiO_{2-x}/MCN as shown in Fig. 1b, S7, 8. The characteristic stretch vibration peaks of g-C₃N₄ are observed, demonstrating the existence of g-C₃N₄ structure in the composites. The broad peak at 3160 cm^{-1} is assigned to the N–H stretching mode in the g-C₃N₄ structure, while the absorption peak at 1575 and 1640 cm^{-1} are related to the C=N stretching vibration. The characteristic absorption peaks centered at 1237, 1316 and 1401 cm^{-1} are ascribed to the characteristic stretching vibration modes of the C–NH units of g-C₃N₄ [49]. However, the absorption peaks of the C–NH bonds for yTiO_{2-x}/MCN and 2TiO₂-MCN are both blue-shifted to 1249, 1332 and 1414 cm^{-1} . At the same time, the peak at 807 cm^{-1} ascribed to aromatic C–N stretching of the tri-s-triazine units is also blue-shifted to 810 cm^{-1} . The above results indicate a decrease in the electron cloud density of C–N bond, probably due to the formation of new chemical bond at the interface of TiO₂ and g-C₃N₄ [26,50]. X-ray photoelectron spectroscopy (XPS) was further used to examine the chemical states of elements in the samples. The survey XPS spectra affirmed the existence of TiO₂ in the heterostructure (Fig. S9). TiO₂/MCN possesses C and N chemical states similar to those of MCN as shown in the high-resolution XPS spectra of C1s and N1s (Fig. S10, 11). The XPS spectrum of Ti 2p for the M-TiO₂ contains two individual peaks located at 458.5 and 464.1 eV (Fig. 2c), corresponding to the Ti 2p_{3/2} and Ti 2p_{1/2} binding energy of the Ti-O-Ti bonds [51]. The Ti 2p peaks of yTiO_{2-x}/MCN were fit to four peaks at 457.9, 458.5, 463.5 and 464.1 eV, corresponding to Ti³⁺ 2p_{3/2}, Ti⁴⁺ 2p_{3/2}, Ti³⁺ 2p_{1/2} and Ti⁴⁺ 2p_{1/2}, respectively, revealing the existence of Ti³⁺ in yTiO_{2-x}/MCN and, indirectly, the presence of oxygen vacancies [52–54]. By contrast, the Ti 2p XPS spectrum of 2TiO₂-MCN revealed that the two individual peaks were in the same locations as for M-TiO₂, indicating that no oxygen vacancies were formed. In addition, the O 1s XPS spectrum of M-TiO₂ displays two peaks (Fig. 2d) located at 529.7 and 531.4 eV, corresponding to O-Ti bond and O-atom near the oxygen vacancy in imperfect TiO₂ [55,56]. The peak area at 531.4 eV in yTiO_{2-x}/MCN is remarkably greater than that of M-TiO₂, confirming the high concentration of oxygen vacancies in yTiO_{2-x}/MCN. Moreover, the peak at 529.7 eV in yTiO_{2-x}/MCN shifts to a lower binding energy, while, no obvious difference is observed in

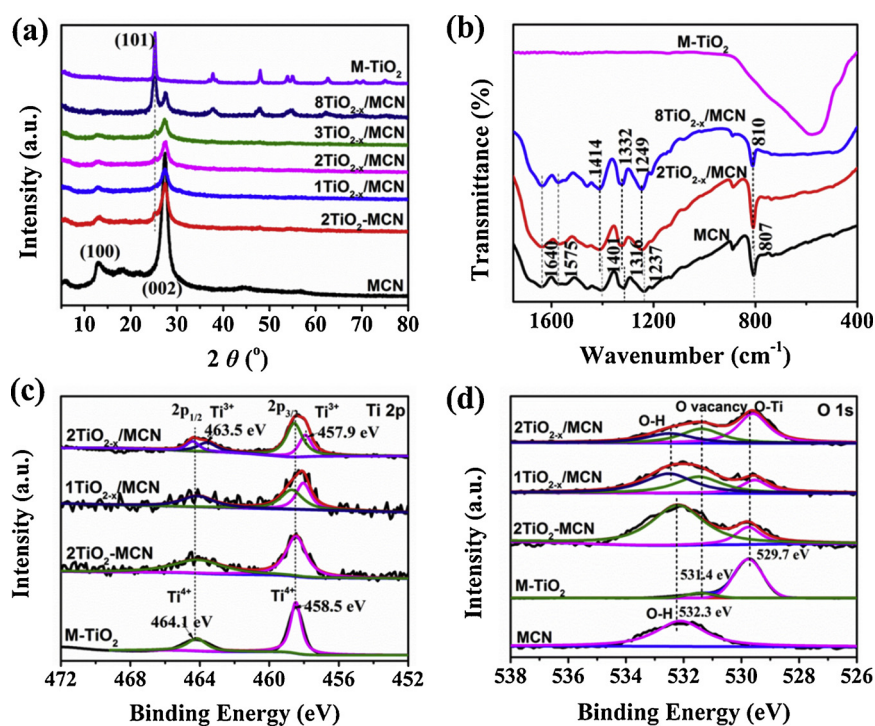
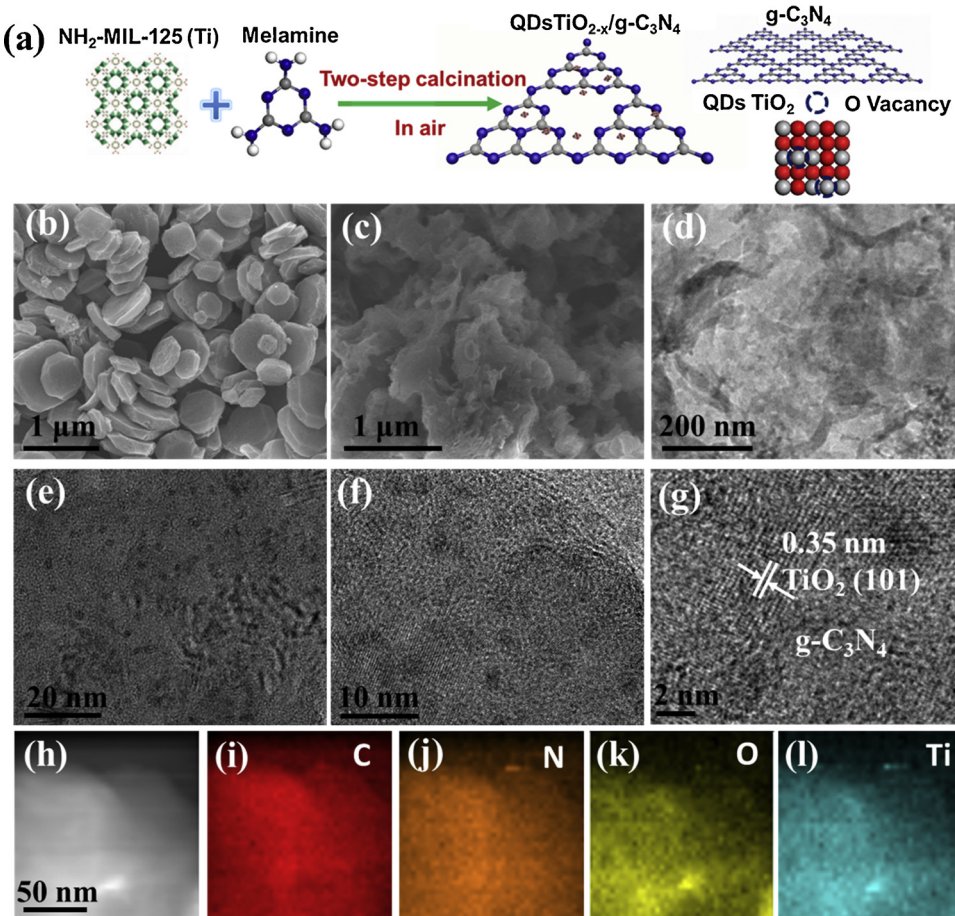


Fig. 2. (a) XRD patterns of MCN, M-TiO₂, $y\text{TiO}_{2-x}/\text{MCN}$ and $2\text{TiO}_2/\text{MCN}$. (b) FT-IR spectra of MCN, M-TiO₂, $y\text{TiO}_{2-x}/\text{MCN}$. (c, d) XPS Ti 2p and O 1s spectra of $g\text{-C}_3\text{N}_4$, pure TiO_2 , $y\text{TiO}_{2-x}/\text{MCN}$ and $2\text{TiO}_2/\text{MCN}$.

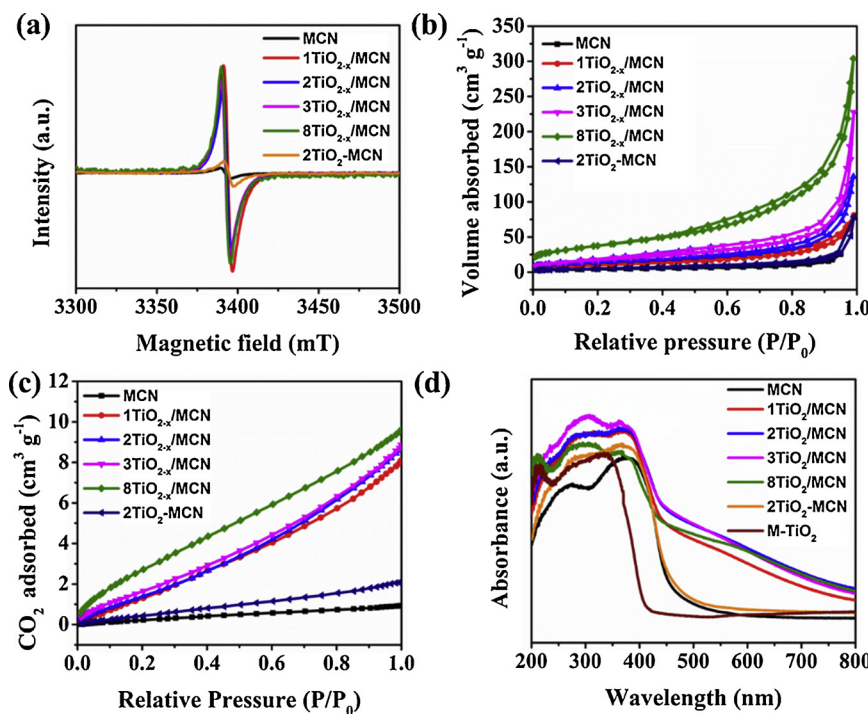


Fig. 3. (a) EPR spectra, (b) N₂ adsorption-desorption isotherms, (c) CO₂ adsorption isotherms, (d) UV-vis diffuses reflectance spectra of MCN, yTiO_{2-x}/MCN and 2TiO₂-MCN.

the peaks at 529.4 and 532.3 eV (attributed to O–H groups) in 2TiO₂-MCN compared with M-TiO₂ and MCN. This result further demonstrates the formation of oxygen vacancies in yTiO_{2-x}/g-C₃N₄ and the presence of interfacial effects in the heterostructure [57].

Electron paramagnetic resonance (EPR) spectroscopy is also an effective approach to directly detect the oxygen vacancies. As shown in Fig. 3a, for MCN, the weak EPR signal assigned to $g \sim 2.003$ was ascribed to the unpaired electron localized at the carbon atom in a typical heptazine of g-C₃N₄ [58]. The previous reports elucidated the EPR signal at $g \sim 2.001\text{--}2.004$ for the oxygen vacancies in TiO₂ [56,59,60]. The g value is very approximate in both unpaired electrons of g-C₃N₄ and oxygen vacancies of TiO₂. However, compared with 2TiO₂-MCN (which has the EPR signal intensity similar to that of MCN), the much stronger EPR intensities with $g \sim 2.002$ were observed in yTiO_{2-x}/MCN. This compared result suggests that the existence of defects is mostly ascribed to oxygen vacancies in the TiO₂ particles rather than the defects of g-C₃N₄.

N₂ adsorption-desorption isotherms of the pristine g-C₃N₄ and yTiO_{2-x}/MCN were shown in Fig. 3b. All exhibit the type IV-H₃ type hysteresis loops. Obviously, yTiO_{2-x}/MCN show much higher N₂ volume adsorption compared with MCN and 2TiO₂-MCN, and the surface area and pore volume are listed in Table S1. The largest surface area in yTiO_{2-x}/MCN is almost ten times larger than that of pristine g-C₃N₄ ($14.4 \text{ m}^2 \text{ g}^{-1}$ and $0.039 \text{ cm}^3 \text{ g}^{-1}$). However, the surface area and pore volume of 2TiO₂-MCN are approximately equal to those of MCN. The pore size distribution (Fig. S12) further indicates the production of mesopores and even macropores due to the release of large amount of gas (NH₃ and CO₂) insitu pyrolysis process. Due to the large surface area and pore volume, yTiO_{2-x}/MCN also exhibits superior CO₂ adsorption ability in comparison with MCN and 2TiO₂-MCN as shown in Fig. 3c. The adsorption volume of CO₂ for yTiO₂/MCN ($8\text{--}10 \text{ cm}^3 \text{ g}^{-1}$) was also ten times larger than that of MCN ($0.8 \text{ cm}^3 \text{ g}^{-1}$), which is advantageous for CO₂ conversion.

The optical properties of yTiO_{2-x}/MCN were evaluated by UV-vis diffuse reflectance spectroscopy as shown in Fig. 3d. The composite of TiO₂/g-C₃N₄ is more responsive to the visible light than M-TiO₂. yTiO_{2-x}/MCN exhibit enhanced visible light absorption, attributable to

the defects in the composite. It has been reported that oxygen defects in metal oxide lattices can enhance visible light absorption and greatly lower the barrier to photocatalytic reactions [52,54,61]. In addition, the band gaps were estimated from the Kubelka–Munk function versus photon energy as listed in Table S1, based on UV-vis diffuse reflectance spectra. An apparent red-shifted absorption edge is observed for yTiO_{2-x}/MCN ($y = 1\text{--}3$) and the band gap decreases with increasing dosage of Ti-MOF. The narrowed band gap is ascribed to the presence of oxygen vacancies in yTiO_{2-x}/MCN. However, 8TiO_{2-x}/MCN shows the opposite tendency, indicating the dominant role of the optical properties of TiO₂ over the oxygen vacancy effect.

3.2. Photoreduction CO₂ activity

The photocatalytic CO₂ reduction performance was evaluated in the mixture of MeCN/TEOA with cocatalyst of Co(bpy)₃²⁺ under visible light irradiation [62]. M-TiO₂ had almost no photocatalytic CO₂ conversion activity. As shown in Fig. 4a, 2TiO₂-MCN showed higher CO evolution than MCN. This difference is attributed to higher CO₂ adsorption ability and the interface effect triggered charge transfer. yTiO_{2-x}/MCN samples all exhibited excellent photocatalytic CO₂ reduction performance compared with MCN and 2TiO₂-MCN. The CO evolution ($388.9 \mu \text{ mol g}^{-1}$) of 2TiO_{2-x}/MCN was higher than those of other samples (no obvious difference in CO evolution for $x = 1, 3$ and 8TiO_{2-x}/MCN) and five times higher than that of MCN ($75.3 \mu \text{ mol g}^{-1}$) in 5 h. These results indicate that the remarkable CO₂ photoreduction performance should be related to the unique structures and surface or interface composition of OD/2D heterostructure such as defects in the material as well as large surface area and pore volume for increasing CO₂ adsorption and promoting charge separation. In addition, we detected both gas and liquid phase products and found that except product of CO, no CH₄, CH₃OH and HCOOH were produced. Only a small amount of H₂ was detected in our experiments, and the distribution of products is shown in Fig. 4b and Table S1. Compared with MCN, the selectivity of 2TiO₂-MCN was almost unchanged, while yTiO_{2-x}/MCN showed a slight decrease in selectivity of CO with increasing Ti-MOF dosage, indicating that more TiO₂ is disadvantageous for CO evolution.

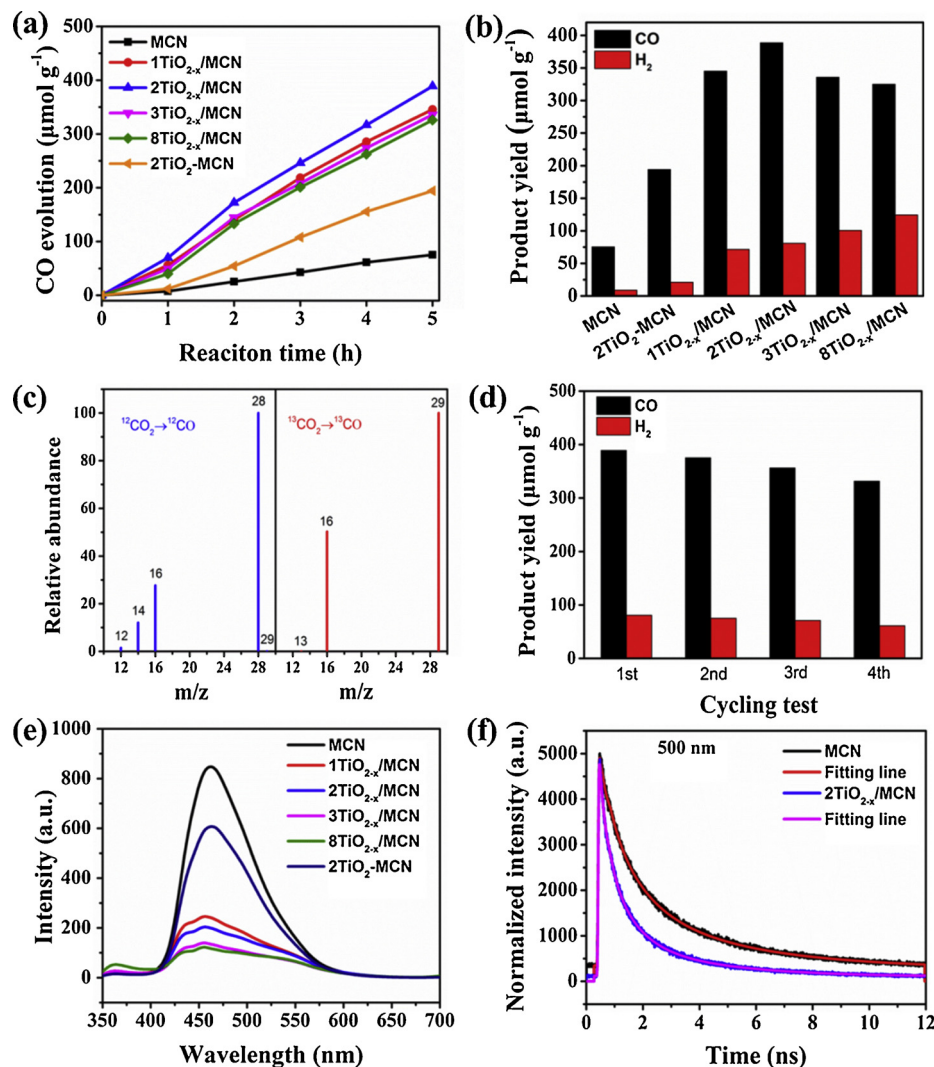


Fig. 4. (a, b) CO evolution and CO and H₂ distribution for MCN, $y\text{TiO}_{2-x}/\text{MCN}$ and 2TiO₂-MCN. (c) Results of GC-MS analysis of ¹²CO and ¹³CO. (d) CO and H₂ evolution distribution for 2TiO_{2-x}/MCN in cycling test, each cycle for 5 h. (e) Steady PL spectra with 310 nm excitation. (f) Time-resolved fluorescence decay spectra of MCN and 2TiO_{2-x}/MCN probed at 500 nm by time-correlated single-photo counting. The samples were excited by incident light of 400 nm from a picosecond pulsed light emitting diode.

Moreover, the CO yields for TiO₂/g-C₃N₄ in one-step pyrolysis were lower than those for TiO_{2-x}/MCN (Fig. S13), indicating that good crystallinity and the uniform distribution of TiO₂ quantum dots favor CO and H₂ evolution.

Control experiments demonstrated that no product was detected if the CO₂ conversion reaction was carried out in the absence of the photocatalyst or light source. Meanwhile, no obvious CO generation was observed without TEOA or CO₂ replaced by Ar (Fig. S14). Thus, CO₂ was considered the sole carbon source of the CO products, which was further verified by ¹³C isotope test (Fig. 4c). Having established the high activity of TiO_{2-x}/MCN, another key parameter of catalytic performance, stability, was evaluated. Recycled of 2TiO_{2-x}/MCN still maintained approximately 85% of its initial activity after four cycling runs (each run for 5 h) (Fig. 4d). From the XRD patterns and FT-IR spectra of the used catalyst (Figs. S15 and 16), the basic framework of photocatalyst still remains. The decreased peak intensity of XRD patterns of used photocatalyst could be assigned to very small amount of recyclable sample for XRD test. The stability of TiO_{2-x}/MCN shows the potential as photocatalyst for realizing CO₂ conversion.

3.3. Steady charge separation efficiency

To further clarify the difference in photocatalytic performance of between MCN and TiO_{2-x}/MCN, steady photoluminescence (PL) spectroscopy was carried out to investigate photoinduced charge separation. MCN showed a high-intensity fluorescence signal at 460 nm due to band-band transition while significantly decreased PL intensity is observed for $y\text{TiO}_{2-x}/\text{MCN}$ and the intensity gradually decreased with increasing TiO₂ amount (Fig. 4e). The obvious PL quenching indicates that the charge transfer process takes place in a nonradiative pathway in the interface between both of materials, consequently, leading to efficient charge migration and separation [63,64]. Transient photocurrent tests and electrochemical impedance spectroscopy (EIS) were also applied to measure the charge separation efficiency. Transient photocurrent results reveal that TiO_{2-x}/MCN exhibits enhanced photocurrent response compared with MCN and 2TiO₂-MCN (Fig. S17), suggesting promoted separation and transport of photogenerated electron-hole pairs. The EIS spectra also manifest a much smaller arc radius for 2TiO_{2-x}/MCN compared with 2TiO₂-MCN and MCN (Fig. S18), demonstrating a low charge-transport resistance for fast interfacial charge transfer separation. This great charge separation efficiency could be another reason for the enhanced photocatalytic CO₂ reduction activity

Table 1Decay lifetimes of tr-PL, fs-TA and ns-TA spectra and their relative percentages of photoexcited charge carriers in the g-C₃N₄ and 2TiO_{2-x}/MCN.

Method	Sample	λ^a , nm	τ_1^b	A ₁ % ^c	τ_2	A ₂ %	τ_3	A ₃ %
tr-PL $\lambda_{\text{ex}} = 400$ nm	MCN	500	0.35 ns	25	1.2 ns	45	4.1 ns	30
	2TiO _{2-x} /MCN	500	0.26 ns	46	0.9 ns	40	3.7 ns	14
fs-TA $\lambda_{\text{ex}} = 350$ nm	MCN	500	2.0 ps	-34	45 ps	-36	4900 ps	-30
	2TiO _{2-x} /MCN	500	0.6 ps	-32	31 ps	-36	> 5000 ps	-32
ns-TA $\lambda_{\text{ex}} = 355$ nm	MCN	430	96 ns	75	28 μ s	25	-	-
	2TiO _{2-x} /MCN	430	58 ns	97	6.6 μ s	3	-	-

^a λ represents probed wavelength.^b τ is referred to decay lifetime.^c A represents amplitude of decay.

of yTiO_{2-x}/MCN in addition to the superior CO₂ adsorption volume and enhanced visible light absorption.

3.4. Charge transfer dynamics and photocatalytic mechanism

To further explain the superior charges separation of yTiO_{2-x}/MCN, time-resolved photoluminescence (tr-PL) and transient absorption (TA) spectra were performed to measure the charge separation dynamics. We first examined the fluorescence lifetime of charge carriers by time-correlated single-photo counting (TCSPC) as shown in Fig. 4f. Both spectra showed multi-exponential decay and the overall decay of 2TiO_{2-x}/MCN is faster than that of MCN. Deconvolution of the decay spectra gave the three lifetimes of charge carriers as listed in Table 1. The three lifetimes of the charge carriers were attributed to intraplanar, interplanar, or intrachain free polarons hopping transport of singlet excitons with subsequent electron-hole recombination [65]. The population of short-lived charge carriers (less than 1 ns) is dominant for 2TiO_{2-x}/MCN resulting in rapid recombination of photoinduced electron–hole pairs. Compared with MCN, the amplitude of short-lived charges (less than 0.5 ns) increased from 25% to 46% and the amplitude of long-lived charges decreased from 30% to 14% in 2TiO_{2-x}/MCN. This result implies that the establishment of channels of electron transfer from g-C₃N₄ to TiO₂ (assuming electron transfer from the conduction

band (CB) of g-C₃N₄ to the CB of TiO₂) thus quenching the emission and leading to faster decay [66,67], in accordance with steady-PL results.

To further certify the charge transfer, transient absorption spectroscopy was performed over eight orders of magnitude in the time scale. First, femtosecond pump-probed transient absorption (fs-TA) spectra reveal a ground state bleaching signal peaking at 500 nm for both materials as shown in Fig. 5a, b, which is assigned to the simulated emission [65,68]. The decay kinetics profiles of the fs-TA spectra (Fig. S19) probed at 500 nm were fitted by three-exponential decay and the lifetimes are listed in Table 1. Three decay lifetimes of (2.0 ps, -34%), (45 ps, -36%) and (4900 ps, -30%) are monitored for MCN, attributed to the photogenerated electron and hole recombination and non-radiation relaxation [69,70]. Importantly, a much shorter lifetime of charge carriers (0.6 ps, -32%) is observed for 2TiO_{2-x}/MCN. The ultrafast lifetime of charge carriers should be attributed to interfacial charge transfer, which takes place within < 1 ps. Similar charge transfer situations have been reported in other systems, such as CdSe/Au [66], CdSe/TiO₂ [69], Pt/TiO₂ [70], and BP/CN [23], in which electrons transfer usually occurs in an ultrafast time scale (fs-ps). Because of the interfacial effect in TiO_{2-x}/MCN, OD-TiO₂ acts as the channel for electron acceptance from the CB of g-C₃N₄, leading to efficient charge separation.

The absorption of the longer-lived charges was further measured by

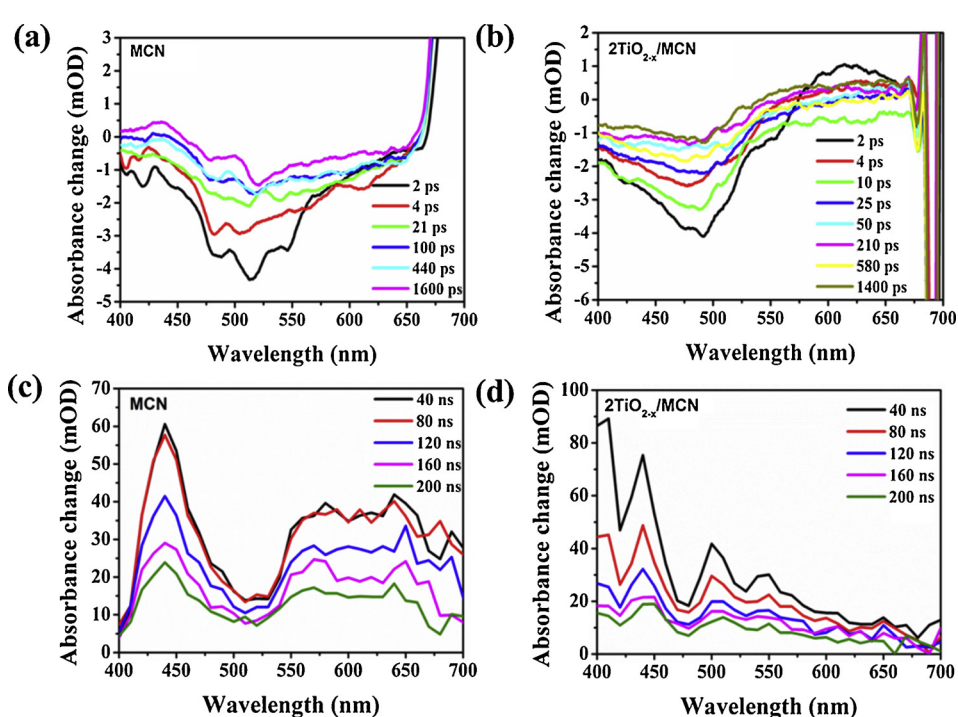


Fig. 5. (a, b) fs-TA spectra of MCN and 2TiO_{2-x}/MCN dispersions (2 mg/mL) probed at 500 nm with 350 nm excitation, (c, d) ns-TA spectra of MCN and 2TiO_{2-x}/MCN dispersions (0.1 mg/mL) probed at 430 nm with 355 nm excitation.

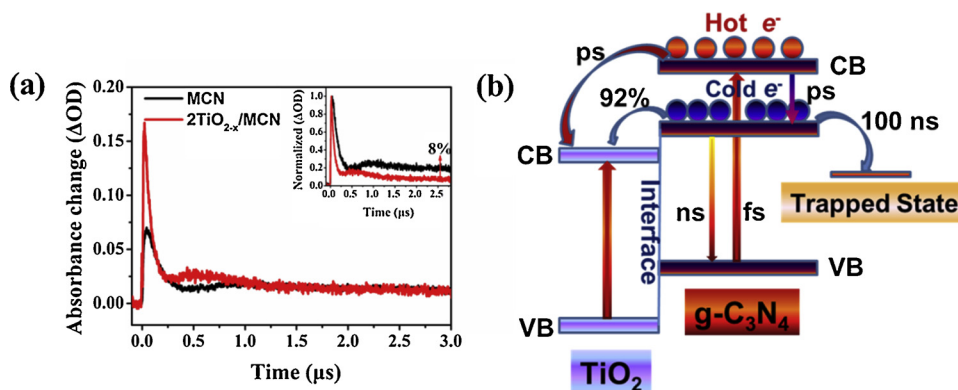


Fig. 6. (a) Decay dynamics fitting curves of MCN and 2TiO_{2-x}/MCN dispersions (0.1 mg/mL aqueous) probed at 430 nm with 355 nm excitation, normalized TA time trace of MCN and 2TiO_{2-x}/MCN was inset. (b) Proposed schematic of band alignment of TiO₂/g-C₃N₄. Electrons are excited from ground state (GS) to excited state (ES) (fs) with 355 nm excess energy to form hot electrons. Hot electrons release energy and return to the bottom of CB (ps) via intraband relaxation. At the same time, hot electrons transfer in TiO₂ particles. The electrons can be trapped in defect sites or vicinal materials (100 ns). Moreover, after cold electron transfer, 8% of photoinduced charges remain in the 2TiO_{2-x}/MCN (μs).

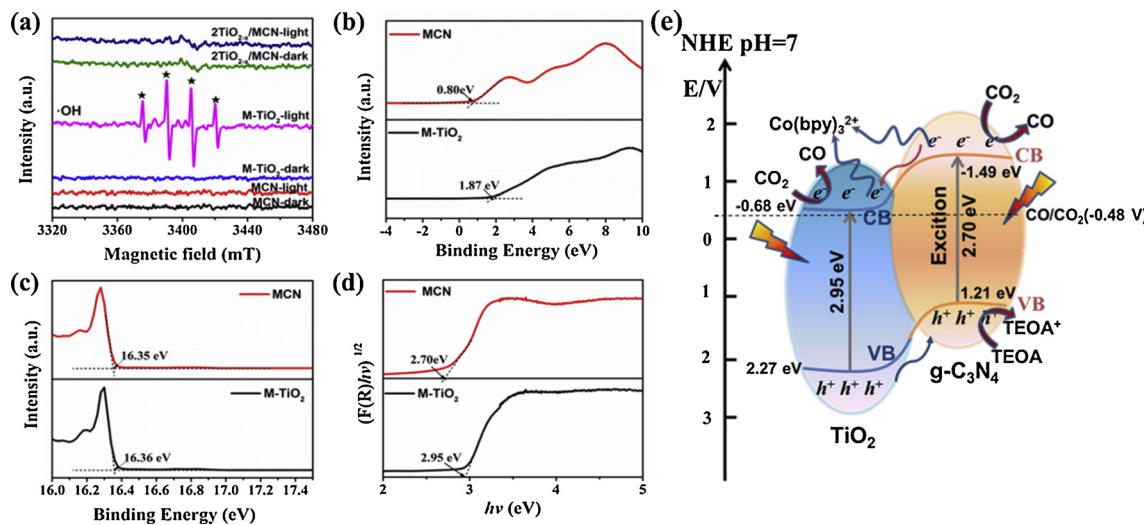


Fig. 7. (a) EPR spectra of hydroxyl radical test in water solvents with DMPO (50 mM) as radical trapper for MCN, M-TiO₂ and 2TiO_{2-x}/MCN under dark and light conditions. (b) Fermi level edges obtained by UPS. (c) Secondary electron cutoff of UPS spectra ($h\lambda_{exc} = 21.2$ eV). (d) Optical band gaps determined by UV/Vis diffuse reflectance spectroscopy (Fig. 3d). (e) Schematic of the electronic structure of g-C₃N₄ and TiO₂ via photocatalytic CO₂ reduction. TEOA is electron donor and Co(bpy)₃²⁺ functions as electron mediator.

nanosecond transient absorption (ns-TA) spectroscopy. Both MCN and 2TiO_{2-x}/MCN showed a broad absorption in the visible region at 430–700 nm region (Fig. 5c, d). The charge decay always exhibits the positive absorption signal from 40 ns to 200 ns, even to 5 μs (Fig. S20), which is due to geminate recombination and bimolecular recombination [65,68], respectively. The decay curves were fitted by two-exponential decay as shown in Fig. 6a and the lifetimes are summarized in Table 1. Obviously, the short-lived charges (58 ns, 97%) are predominant for 2TiO_{2-x}/MCN and the lifetime is much shorter than that of MCN (120 ns, 75%). The lifetime of long-lived charges in 2TiO_{2-x}/MCN (6.6 μs, 3%) was also much shorter than that of MCN (28 μs, 25%). These results also indicate that electron transfer occurs in the interface of the heterostructure thus giving rise to a faster dominant decay of charges. This also suggests that the charges are shallow trapped [69], which is in favor of electrons trapped by CO₂ to form CO₂⁻. In addition, one could speculate that approximately 8% of electrons remained in 2TiO_{2-x}/MCN compared with MCN (20%), which further verifies the formation of electron transfer from 2D-g-C₃N₄ to QDs TiO₂ resulting in less residual electrons and a much shorter lifetime of charges [66]. Hence, the charge separation and transfer mechanism are described in Fig. 6b. Rapid excitation (< 200 fs) leads to dissociation into singlet polaron pairs [65]. The excess energy of 355 nm excitation compared with 500 nm probed is anticipated to bring valence electrons up to states above the CB edge of 2D-g-C₃N₄, and generate the so-called hot electrons. Subsequently, the hot electrons release the excess energy via intraband relaxation to return to the bottom of CB and are then, called

cold electrons [66,71]. At the same time, the hot electrons transfer to the CB of 0D-TiO₂ through the heterojunction interface, which is a very ultrafast process (< 1 ps). Furthermore, the hot electron transfer usually competes with intraband relaxation. 0D-TiO₂ can significantly enhance charge separation by accepting the hot and cold electrons transferred from 2D-g-C₃N₄. The electrons can also be trapped in the defect sites to enable the charge carrier separation (100 ns). After cold electron transfer, 8% of photoinduced electrons remain in TiO_{2-x}/MCN at a microsecond time scale. Based on this discussion, fast electron transfer greatly enhances charge separation and thus significantly promotes photocatalytic CO₂ reduction activity.

To establish the photocatalytic mechanism, it is imperative to certify the charge transfer direction. Therefore, electron paramagnetic resonance (EPR) spectra were performed to detect hydroxyl radicals ('OH) by use of water solvent with dimethyl pyridine N-oxide (DMPO) as the radical trapper. As shown in Fig. 7a, no obvious 'OH signals are observed for MCN under dark and light irradiation, suggesting that the position of VB for MCN is not positive enough for H₂O or OH⁻ oxidation to 'OH. M-TiO₂ shows a strong 'OH signal under light irradiation and no signals under dark, indicating that H₂O or OH⁻ was oxidized to 'OH over M-TiO₂. However, no evident signals were detected in TiO_{2-x}/MCN under either dark or light conditions. This demonstrates that holes migrate in the direction from the valence band (VB) of TiO₂ to the VB of g-C₃N₄, but H₂O or OH⁻ cannot be oxidized to 'OH on the potential of VB of g-C₃N₄. These results make clear that charge transfer is the typical route, i.e., electrons transfer from the CB of g-C₃N₄ to the CB of TiO₂,

and holes transfer from the VB of TiO_2 to the VB of $\text{g-C}_3\text{N}_4$.

To outline the VB and CB positions in detail, the UPS spectra of pure $\text{g-C}_3\text{N}_4$ (MCN) and M- TiO_2 were measured. By using the method of linear approximation to the UPS spectra (Fig. 7b,c), the VB maximums (E_{VB}) for MCN and M- TiO_2 were calculated to be -5.65 and -6.71 eV versus the vacuum level, respectively (Supporting Information). In addition, according to the relationship between the vacuum energy level and the potential of the normal hydrogen electrode (NHE), $E_{\text{VB}}^* = -E_{\text{VB}} - 4.44$, the VB of MCN and M- TiO_2 were calculated as 1.21 and 2.27 eV, respectively. Combined with the band gaps obtained from the Tauc plots (Fig. 7d), the CB positions were calculated to be -1.49 and -0.68 eV, respectively. As a result, the energy band alignment of $\text{g-C}_3\text{N}_4$ and M- TiO_2 (Fig. 7e) illustrates the charges transfer process, indicating an in-depth understanding of photocatalytic CO_2 reduction mechanism via the use of 0D/2D heterostructures.

4. Conclusions

In summary, we have successfully synthesized 0D/2D heterostructures of oxygen vacancy-rich TiO_2 quantum dots confined in $\text{g-C}_3\text{N}_4$ nanosheets by in-situ pyrolysis of $\text{NH}_2\text{-MIL-125}$ (Ti) and melamine, and described the interfacial electron transfer in the typical way. The obtained $\text{TiO}_{2-x}/\text{MCN}$ materials exhibit advantages of enhanced visible light absorption, superior CO_2 adsorption, large surface area and efficient charge separation, thus significantly enhancing photocatalytic CO_2 reduction activity. Charge dynamics analysis by time-resolved photoluminescence and femtosecond and nanosecond pump-probed transient absorption spectra reveals that the overall fast decays of the charge carriers in $\text{TiO}_{2-x}/\text{MCN}$ are due to charge transfer from 2D- $\text{g-C}_3\text{N}_4$ to 0D- TiO_2 through the heterojunction interface. Electron transfer takes place in an ultrafast subpicosecond time scale and is subsequently accompanied by recombination relaxation mediated by shallow trapped sites. The fast charge transfer greatly promotes charge separation and suppression of photogenerated charge recombination in 0D/2D $\text{TiO}_{2-x}/\text{g-C}_3\text{N}_4$ heterostructure. The present work provides guidelines for understanding the charge transfer mechanism and engineering the intimate heterojunction interface for efficient charge transfer, thus promoting the development of high-performance photocatalysts for energy conversion.

Acknowledgment

This work was financially supported by the National Key Research and Development Program of China (2016YFB0600902-5).

Appendix A. Supplementary data

Supplementary material related to this article can be found, in the online version, at doi:<https://doi.org/10.1016/j.apcatb.2019.01.036>.

References

- [1] C. Gao, S. Chen, Y. Wang, J. Wang, X. Zheng, J. Zhu, L. Song, W. Zhang, Y. Xiong, *Adv. Mater.* 30 (2018) 1704624–1704632.
- [2] A. Iwase, S. Yoshino, T. Takayama, Y.H. Ng, R. Amal, A. Kudo, *J. Am. Chem. Soc.* 138 (2016) 10260–10264.
- [3] T.T. Zhuang, Y. Liu, Y. Li, Y. Zhao, L. Wu, J. Jiang, S.H. Yu, *Angew. Chem. Int. Ed.* 55 (2016) 6396–6400.
- [4] R. Kuriki, M. Yamamoto, K. Higuchi, Y. Yamamoto, M. Akatsuka, D. Lu, S. Yagi, T. Yoshida, O. Ishitani, K. Maeda, *Angew. Chem. Int. Ed.* 56 (2017) 4867–4871.
- [5] R. Kuriki, H. Matsunaga, T. Nakashima, K. Wada, A. Yamakata, O. Ishitani, K. Maeda, *J. Am. Chem. Soc.* 138 (2016) 5159–5170.
- [6] M.G. Walter, E.L. Warren, J.R. McKone, S.W. Boettcher, Q. Mi, E.A. Santori, N.S. Lewis, *Chem. Rev.* 110 (2010) 6446–6473.
- [7] Q. Yuan, D. Liu, N. Zhang, W. Ye, H. Ju, L. Shi, R. Long, J. Zhu, Y. Xiong, *Angew. Chem. Int. Ed.* 56 (2017) 4206–4210.
- [8] X. Wang, S. Blechert, M. Antonietti, *ACS Catal.* 2 (2012) 1596–1606.
- [9] X. Wang, K. Maeda, X. Chen, K. Takanabe, K. Domen, Y. Hou, X. Fu, M. Antonietti, *J. Am. Chem. Soc.* 131 (2009) 1680–1681.
- [10] D. Zheng, C. Pang, Y. Liu, X. Wang, *Chem. Commun.* 51 (2015) 9706–9709.
- [11] J. Qin, S. Wang, H. Ren, Y. Hou, X. Wang, *Appl. Catal. B Environ.* 179 (2015) 1–8.
- [12] L. Lin, W. Ren, C. Wang, A. Asiri, J. Zhang, X. Wang, *Appl. Catal. B Environ.* 231 (2018) 234–241.
- [13] X. Wang, K. Maeda, A. Thomas, K. Takanabe, G. Xin, J.M. Carlsson, K. Domen, M. Antonietti, *Nat. Mater.* 8 (2009) 76–80.
- [14] Y. Fang, X. Wang, *Chem. Commun.* 54 (2018) 5674–5687.
- [15] J. Sun, J. Zhang, M. Zhang, M. Antonietti, X. Fu, X. Wang, *Nat. Commun.* 3 (2012) 1139–1145.
- [16] Y. Cui, Z. Ding, X. Fu, X. Wang, *Angew. Chem. Int. Ed.* 51 (2012) 11814–11818.
- [17] Y. Zheng, L. Lin, X. Ye, F. Guo, X. Wang, *Angew. Chem. Int. Ed.* 53 (2014) 11926–11930.
- [18] Z. Lin, X. Wang, *Angew. Chem. Int. Ed.* 125 (2013) 1735–1738.
- [19] L. Lin, Z. Yu, X. Wang, *Angew. Chem. Int. Ed.* (2018), <https://doi.org/10.1002/anie.201809897>.
- [20] J. Zhang, F. Guo, X. Wang, *Adv. Funct. Mater.* 23 (2013) 3008–3014.
- [21] G.P. Mane, D.S. Dhawale, C. Anand, K. Ariga, Q. Ji, M.A. Wahab, T. Mori, A. Vinu, *J. Mater. Chem. A* 1 (2013) 2913–2920.
- [22] P. Yang, R. Wang, M. Zhou, X. Wang, *Angew. Chem. Int. Ed.* 57 (2018) 8674–8677.
- [23] M. Zhu, S. Kim, L. Mao, M. Fujitsuka, J. Zhang, X. Wang, T. Majima, *J. Am. Chem. Soc.* 139 (2017) 13234–13242.
- [24] K. Wei, K. Li, L. Yan, S. Luo, H. Guo, Y. Dai, X. Luo, *Appl. Catal. B Environ.* 222 (2018) 88–98.
- [25] A. Fujishima, *Nature* 238 (1972) 37–38.
- [26] Y. Wang, W. Yang, X. Chen, J. Wang, Y. Zhu, *Appl. Catal. B Environ.* 220 (2018) 337–347.
- [27] J. Hao, S. Zhang, F. Ren, Z. Wang, J. Lei, X. Wang, T. Cheng, L. Li, *J. Colloid Interface Sci.* 508 (2017) 419–425.
- [28] W. Wang, J. Fang, S. Shao, M. Lai, C. Lu, *Appl. Catal. B Environ.* 217 (2017) 57–64.
- [29] H. Wang, Y. Liang, L. Liu, J. Hu, W. Cui, J. Hazard. Mater. 344 (2018) 369–380.
- [30] Y.N. Li, Z.Y. Chen, M.Q. Wang, L.Z. Zhang, S.J. Bao, *Appl. Surf. Sci.* 440 (2018) 229–236.
- [31] H. Wei, W.A. McMaster, J.Z.Y. Tan, L. Cao, D. Chen, R.A. Caruso, *J. Phys. Chem. C* 121 (2017) 22114–22122.
- [32] X. Dai, Z. Zhang, Y. Jin, Y. Niu, H. Cao, X. Liang, L. Chen, J. Wang, X. Peng, *Nature* 515 (2014) 96–99.
- [33] A.P. Alivisatos, *Science* 271 (1996) 933–937.
- [34] A. Boulesbaa, K. Wang, M. Mahjouri-Samani, M. Tian, A.A. Puretzky, I. Ivanov, C.M. Rouleau, K. Xiao, B.G. Sumpter, D.B. Geohegan, *J. Am. Chem. Soc.* 138 (2016) 14713–14719.
- [35] M.Y. Ye, Z.H. Zhao, Z.F. Hu, L.Q. Liu, H.M. Ji, Z.R. Shen, T.Y. Ma, *Angew. Chem. Int. Ed.* 129 (2017) 8407–8411.
- [36] J. Liu, J. Ke, Y. Li, B. Liu, L. Wang, H. Xiao, S. Wang, *Appl. Catal. B Environ.* 236 (2018) 396–403.
- [37] H.L. Wu, Z. Kang, Z.H. Zhang, Z. Zhang, H.N. Si, Q.L. Liao, S.C. Zhang, J. Wu, X.K. Zhang, Y. Zhang, *Adv. Funct. Mater.* 28 (2018) 1802015–1802024.
- [38] Z. Lu, C. Li, J. Han, L. Wang, S. Wang, L. Ni, Y. Wang, *Appl. Catal. B Environ.* 237 (2018) 919–926.
- [39] H.H. Gao, H.C. Yang, J.Z. Xu, S.W. Zhang, J.X. Li, *Small* 14 (2018) 1801353–1801365.
- [40] W. Lei, Y. Mi, R. Feng, P. Liu, S. Hu, J. Yu, X. Liu, J.A. Rodriguez, J.O. Wang, L. Zheng, *Nano Energy* 50 (2018) 552–561.
- [41] Y. Fang, Y. Ma, M. Zheng, P. Yang, A.M. Asiri, X. Wang, *Coord. Chem. Rev.* 373 (2018) 83–115.
- [42] W.W. Zhan, Q.L. Zhu, S. Dang, Z. Liu, M. Kitta, K. Suenaga, L.S. Zheng, Q. Xu, *Small* 13 (2017) 1603879–1603884.
- [43] B. Yan, L. Zhang, Z. Tang, M. Al-Mamun, H. Zhao, X. Su, *Appl. Catal. B Environ.* 218 (2017) 743–750.
- [44] N.D. McNamara, J. Kim, J.C. Hicks, *Energy Fuel* 30 (2015) 594–602.
- [45] S. Joseph, D.M. Kempaiah, B. Benigaz, A.V. Baskar, S.N. Talapaneni, S.H. Jhung, D.-H. Park, A. Vinu, *J. Mater. Chem. A* 5 (2017) 21542–21549.
- [46] J. Yang, F. Zhang, X. Wang, D. He, G. Wu, Q. Yang, X. Hong, Y. Wu, Y. Li, *Angew. Chem. Int. Ed.* 128 (2016) 13046–13050.
- [47] A. Thomas, A. Fischer, F. Goettmann, M. Antonietti, J.O. Mueller, R. Schloegl, J.M. Carlsson, *ChemInfor* 40 (2009) 4893–4908.
- [48] L. Lin, H. Ou, Y. Zhang, X. Wang, *ACS Catal.* 6 (2016) 3921–3931.
- [49] Y. Zheng, L. Lin, X. Ye, F. Guo, X. Wang, *Angew. Chem. Int. Ed.* 126 (2014) 12120–12124.
- [50] X. Hao, J. Zhou, Z. Cui, Y. Wang, Z. Zou, *Appl. Catal. B Environ.* 229 (2018) 41–51.
- [51] W. Wang, W. Huang, Y. Ni, C. Lu, Z. Xu, *ACS Appl. Mater. Interfaces* 6 (2014) 340–348.
- [52] J. Li, M. Zhang, Z. Guan, Q. Li, C. He, J. Yang, *Appl. Catal. B Environ.* 206 (2017) 300–307.
- [53] S. Tan, Z. Xing, J. Zhang, Z. Li, X. Wu, J. Cui, J. Kuang, Q. Zhu, W. Zhou, *J. Catal.* 357 (2018) 90–99.
- [54] X. Yu, X. Fan, L. An, G. Liu, Z. Li, J. Liu, P. Hu, *Carbon* 128 (2018) 21–30.
- [55] F. Lei, Y. Sun, K. Liu, S. Gao, L. Liang, B. Pan, Y. Xie, *J. Am. Chem. Soc.* 136 (2014) 6826–6829.
- [56] J. Wan, W. Chen, C. Jia, L. Zheng, J. Dong, X. Zheng, Y. Wang, W. Yan, C. Chen, Q. Peng, D. Wang, Y. Li, *Adv. Mater.* 30 (2018) 1705369–17053756.
- [57] J. Li, M. Zhang, Z. Guan, Q. Li, C. He, J. Yang, *Appl. Catal. B Environ.* 206 (2017) 300–307.
- [58] G. Liu, G. Zhao, W. Zhou, Y. Liu, H. Pang, H. Zhang, D. Hao, X. Meng, P. Li, T. Kako, *Adv. Funct. Mater.* 26 (2016) 6822–6829.
- [59] S.M. Wu, X.L. Liu, X.L. Lian, G. Tian, C. Janiak, Y.X. Zhang, Y. Lu, H.Z. Yu, J. Hu, H. Wei, H. Zhao, G.G. Chang, G. Van Tendeloo, L.Y. Wang, X.Y. Yang, B.L. Su, *Adv.*

- Mater. (2018) 1802173–1802179.
- [60] X. Feng, P. Wang, J. Hou, J. Qian, Y. Ao, C. Wang, J. Hazard. Mater. 351 (2018) 196–205.
- [61] Y. Ji, Y. Luo, J. Am. Chem. Soc. 138 (2016) 15896–15902.
- [62] J. Lin, Z. Pan, X. Wang, ACS Sustain. Chem. Eng. 2 (2013) 353–358.
- [63] M.-Q. Yang, Y.-J. Xu, W. Lu, K. Zeng, H. Zhu, Q.-H. Xu, G.W. Ho, Nat. Commun. 8 (2017) 14224–14232.
- [64] S. Wang, B.Y. Guan, X.W.D. Lou, J. Am. Chem. Soc. 140 (2018) 5037–5040.
- [65] C. Merschjann, S. Tschierlei, T. Tyborski, K. Kailasam, S. Orthmann, D. Hollmann, T. Schedel-Niedrig, A. Thomas, S. Lochbrunner, Adv. Mater. 27 (2015) 7993–7999.
- [66] P. Yu, X. Wen, Y. Lee, W. Lee, C. Kang, J. Tang, J. Phys. Chem. Lett. 4 (2013) 3596–3601.
- [67] Y. Fang, Y. Xu, X. Li, Y. Ma, X. Wang, Angew. Chem. Int. Ed. 57 (2018) 9749–9753.
- [68] R. Godin, Y. Wang, M.A. Zwijnenburg, J. Tang, J.R. Durrant, J. Am. Chem. Soc. 139 (2017) 5216–5224.
- [69] B.C. Fitzmorris, G.K. Larsen, D.A. Wheeler, Y. Zhao, J.Z. Zhang, J. Phys. Chem. C 116 (2012) 5033–5041.
- [70] Furube Akihiro, Asahi Tsuyoshi, Masuhara Hiroshi, H. Yamashita, M. Anpo, Chem. Phys. Lett. 336 (2001) 424–430.
- [71] V.I. Klimov, J. Phys. Chem. B 104 (2000) 6112–6123.